Pergamon

Int. J. Heat Mass Transfer. Vol. 39, No. 4, pp. 851–865, 1996

0017-9310/96 $15.00+0.00

0017-9310(95)00160-3

Parametric study of buoyancy-induced flow and heat transfer from L-shaped corners with asymmetrically heated surfaces

R. B. CHINNAKOTLA, D. ANGIRASA and R. L. MAHAJAN†

Department of Mechanical Engineering, University of Colorado, Boulder, CO 80309-0427, U.S.A.

(*Received* 4 *May* 1994 *and in final form* 1 *December* 1994)

Abstract—In this concluding companion work to Angirasa *et al.* [*Int. J. Heat Mass Transfer* **37**, 2439–2463 (1994)] a parametric numerical study of two-dimensional (2D) buoyancy-induced flow and heat transfer over L-shaped corners with asymmetric heating is reported. Both the horizontal and vertical surfaces are isothermal and are maintained at different temperatures above ambient temperature. The effect of changing horizontal surface temperature on flow and heat transfer over a square corner is discussed in detail. The influence of aspect ratio (length of horizontal surface : height of vertical surface) is examined. The Prandtl number is shown to have significant influence on flow and transport. For high *Pr*, unsteady flows result with multiple plume formations on the horizontal surface. Nusselt number data are presented for a wide range of parameters studied. Flow visualization using smoke demonstrate interesting flow characteristics revealed by the numerical simulations.

1. INTRODUCTION

Interesting buoyancy-induced flows arise in a corner because of the interaction of flows with different orientations to gravity. Of the several corner configurations [1], the most frequently studied is the L-shaped corner [1–9]. For a detailed survey, see refs. [1] and [9].

Angirasa *et al.* [9] recently presented numerical computations for symmetrically heated L-shaped corners for laminar flows. It was reported that there is a significant reduction in Nusselt number for a vertical surface even for small horizontal surfaces at the leading edge. This is due to the blocking of entrainment flow at the leading edge of the vertical surface and preheating of the fluid by the horizontal surface. They observed unsteady flows for higher Rayleigh numbers. With increase in aspect ratio, changes in the fluid entrainment characteristics were found to be significant.

In the present concluding numerical study, we consider buoyancy-induced flow and heat transfer over isothermal, asymmetrically heated L-shaped corners. The effects of excess temperature ratio, $(t_h - t_\infty)/(t_v - t_\infty)$ and aspect ratio are studied in detail. The influence of Prandtl number is examined for a given Grashof number. Nusselt number data are presented for the corner, and for the horizontal and vertical surfaces. Flow visualizations using smoke support the interesting flow characteristics obtained by numerical simulations.

† Author to whom correspondence should be addressed.

2. ANALYSIS AND NUMERICAL PROCEDURES

Figure 1 shows a schematic diagram of an L-shaped corner. The vertical and horizontal surfaces are aligned with x and y directions, respectively. The height of the vertical surface is L and the length of the horizontal surface is W. The horizontal and vertical surfaces are isothermal and are, respectively, maintained at temperatures t_h and t_v. The ambient temperature is t_∞. The governing equations for two-dimensional (2D), laminar, incompressible buoyancy-induced flows with Boussinesq approximation and constant fluid properties in non-dimensional vorticity-transport form are [9]

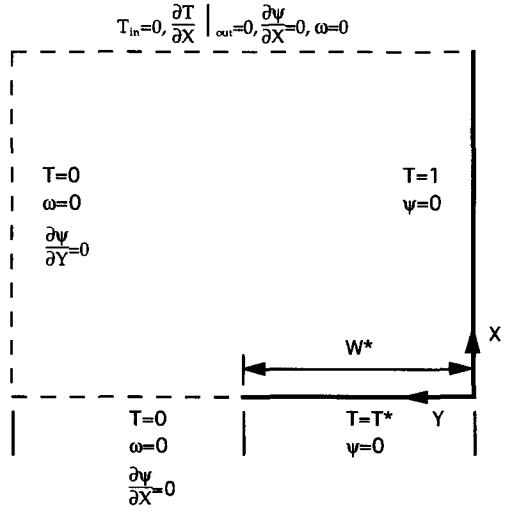

Fig. 1. Numerical boundary conditions.

NOMENCLATURE

g	gravitational acceleration
Gr	Grashof number $= g\beta(t_v - t_\infty)L^3/\nu^2$
k	thermal conductivity of the fluid
L	height of the vertical surface
Nu_h	average Nusselt number for horizontal surface
Nu_L	average Nusselt number for the L-shaped corner
Nu_v	average Nusselt number for vertical surface
p	pressure
P	non-dimensional pressure $= p/\rho U_c^2$
Pr	Prandtl number $= \nu/\alpha$
t	temperature
t_h	horizontal surface temperature
t_v	vertical surface temperature
t_∞	ambient temperature
T	non-dimensional temperature $= (t - t_\infty)/(t_v - t_\infty)$
T^*	horizontal surface excess temperature ratio $= (t_h - t_\infty)/(t_v - t_\infty)$
u	velocity component in x-direction
U_c	reference convective velocity $= \sqrt{[g\beta(t_v - t_\infty)L]}$
U	non-dimensional velocity component in x-direction $= u/U_c$
v	velocity component in y-direction
V	non-dimensional velocity component in y-direction $= v/U_c$
W	length of the horizontal surface
W^*	non-dimensional length of horizontal surface (aspect ratio of the corner) $= W/L$
x, y	space coordinates in vertical and horizontal directions, respectively
X, Y	non-dimensional space coordinates, x/L and y/L.

Greek symbols

α	thermal diffusivity
β	coefficient of thermal expansion $= -(1/\rho)(\partial\rho/\partial t)_p$
ν	kinematic viscosity
ρ	density
ψ	stream function
τ	time
τ^*	non-dimensional time $= \tau U_c/L$
ω	vorticity.

$$\frac{\partial T}{\partial \tau^*} + U\frac{\partial T}{\partial X} + V\frac{\partial T}{\partial Y} = \frac{1}{\sqrt{(Gr)Pr}}\left[\frac{\partial^2 T}{\partial X^2} + \frac{\partial^2 T}{\partial Y^2}\right] \quad (1)$$

$$\frac{\partial \omega}{\partial \tau^*} + U\frac{\partial \omega}{\partial X} + V\frac{\partial \omega}{\partial Y} = \frac{\partial T}{\partial Y} + \frac{1}{\sqrt{Gr}}\left[\frac{\partial^2 \omega}{\partial X^2} + \frac{\partial^2 \omega}{\partial Y^2}\right] \quad (2)$$

where

$$\omega = \frac{\partial U}{\partial Y} - \frac{\partial V}{\partial X}. \quad (3)$$

A stream function ψ is defined such that

$$U = \partial\psi/\partial Y \quad \text{and} \quad V = -\partial\psi/\partial X. \quad (4)$$

From equations (3) and (4), we obtain

$$\omega = \nabla^2\psi. \quad (5)$$

2.1. *Boundary conditions*

The relevant non-dimensional boundary conditions are

$$Y = 0 \quad 0 < X \leqslant 1 \quad U = 0 \quad V = 0 \quad T = 1$$

$$X = 0 \quad 0 < Y \leqslant W^* \quad U = 0 \quad V = 0$$

$$T = T^* = \frac{t_h - t_\infty}{t_v - t_\infty}$$

$$Y \to \infty \quad U = 0 \quad T = 0. \quad (6)$$

where $W^* = W/L$ is the aspect ratio of the L-corner. The temperature excess ratio, T^* appears in the boundary conditions. Its value determines the relative heating effects of the horizontal and vertical surfaces. For $t_v > t_h$, $T^* < 1.0$, and vice versa. The corner point (0,0) does not appear in numerical calculations.

2.2. *Evaluation of Nusselt number*

The average Nusselt numbers for vertical and horizontal surfaces are obtained as follows

$$Nu_v = \int_0^1 \left[-\frac{\partial T}{\partial Y}\right]_{Y=0} dX \quad (7)$$

$$Nu_h = \int_0^{W^*} \left[-\frac{\partial T}{\partial X}\right]_{X=0} dY. \quad (8)$$

The average Nusselt number for the L-corner is defined as

$$Nu_L = (Nu_h + Nu_v)/(1 + W^*). \quad (9)$$

The numerical scheme deployed is based on that in refs. [9–11] and the discretization, convergence tests, time-step and error estimates are those in [9]. The numerical boundary conditions and the computational domain are shown in Fig. 1. Following numerical experimentation in refs. [1] and [9], the appropriate computational domain in Y-direction for this problem is chosen as follows: $Y_{max} = 0.5$ for $W^* \leqslant 0.25$ and $Y_{max} = 2W^*$ for $W^* > 0.25$. There is no necessity, however, to extend the computational domain in X-direction beyond $X_{max} = 1.0$. The outflow at X_{max} has the boundary layer characteristics and the outflow boundary conditions given in Fig. 1 accurately describe it. The inflow is essentially the

entrainment flow. The boundary conditions for the inflow, as given in Fig. 1, do not alter the flow in any significant way, see the previous studies [1, 9].

3. RESULTS AND DISCUSSION

Computations were performed for a range of T^* and W^*. The influence of T^* on the flow and heat transfer from a square corner is considered first. It is followed by a discussion on the effect of W^* for $T^* < 1$ and $T^* > 1$. The effect of Prandtl number on flow and transport is then discussed. Finally, flow visualizations are qualitatively compared to the flow patterns obtained by simulations.

3.1. *Effect of horizontal surface temperature*

To study the influence of T^* on flow and transport, T^* was varied from 0.0 to 3.0 for $Gr = 10^6$, $Pr = 0.7$ and $W^* = 1.0$ where $T^* = 0.0$ refers to a cold isothermal horizontal surface at the ambient temperature.

Figure 2 shows the stream function contours for various values of T^*. For the square corner considered, the entrainment for the horizontal flow is from the bottom, and for the vertical flow it is from the top. The entrainment characteristics are similar to those observed by Angirasa *et al.* [9] for $T^* = 1.0$. For $T^* = 0.1$, the fluid entrainment from below the horizontal surface is weak. The velocities on the horizontal surface are low and the flow does not exhibit boundary layer characteristics. The fluid entraining from the ambient below the surface bends and flows over the horizontal surface. The flow adjacent the vertical surface is boundary layer in character. For lower T^*, the boundary layer is mostly fed by the fluid entraining from the top. With increasing T^*, an increase in the buoyant force over the horizontal surface causes higher fluid velocities on the horizontal surface. The horizontal flow turns at the corner and washes the vertical surface. For $T^* > 1.0$, the fluid near the corner is hotter than the vertical surface. It loses thermal energy to the vertical surface. The result is a retardation of the fluid flow which results in a small recirculating–stagnation zone near the corner.

Figure 3 shows the corresponding isotherms. For lower T^*, the isotherms are widely-spaced in the horizontal layer. As T^* increases, these isotherms get closely packed while those adjacent the vertical surface open up. These characteristics are expected from physical considerations. With the warmer fluid feeding the growth of the vertical boundary layer at high T^*, heat transfer from the vertical side is reduced. Also, as pointed out above, for $T^* > 1$, a portion of the vertical surface near the corner gains heat. This is reflected in the Nusselt number of the vertical surface, which we consider next.

Figure 4 presents the variation of Nusselt number for the corner, and for horizontal and vertical surfaces. The value of Nu_v for $T^* = 0$ is in good agreement with that reported in [1] for $W^* = 0.5$. Nu_h increases with T^*. For lower T^*, heat transfer from horizontal surface by convection is weak. The horizontal surface gains more heat near the corner than it loses from the rest of it. The negative value for Nu_h refers to heat gain by horizontal surface. As T^* increases, the induced velocity on the horizontal surface increases causing an increase in Nu_h.

On the other hand, Nu_v decreases with an increase in T^*. As T^* increases, the amount of preheated fluid entering into the vertical boundary layer from the horizontal surface layer increases. This reduces the vertical surface temperature gradients. For $T^* \geqslant 1.0$, the effect of preheating is very significant. It causes vertical surface to gain heat near the corner. For $T^* > 2.0$, the heat transfer from upper part of the vertical surface is more than offset by the heat gain in the lower portion. The net effect is that the vertical surface gains heat for high values of T^*. This is indicated by negative Nu_v. We also note that for $T^* \geqslant 1.5$, the flows are quasi-steady. Periodic, but very small variations are observed in the value of Nu. The results presented in Fig. 4 are time-averaged values after quasi-steady state is reached.

3.2. *Effect of* W*

The effect of W^* on flow and transport is examined for two values of the excess temperature ratio, $T^* = 0.5$ and 2.0. For the former, W^* is varied from 0.1 to 0.75, for the latter, larger values of W^*, up to 3, are investigated.

Stream function contours for $0.1 \leqslant W^* \leqslant 0.75$ with $T^* = 0.5$ are shown in Fig. 5. Gr and Pr are chosen to be 10^6 and 0.7, respectively. For $W^* = 0.1$ and 0.25, fluid entrainment is from the side and the bottom. As W^* increases, entrainment for the vertical boundary layer gradually changes from the side to the top. The horizontal surface always entrains from the bottom. This fluid, after passing over the horizontal surface, changes its direction and feeds the vertical boundary layer at the corner. The entrainment characteristics essentially remain unchanged for higher values of W^*.

Figure 6 shows the corresponding isotherm contours. The vertical surface temperature gradients are slightly steeper near the corner because the horizontal surface gains heat near the corner. It is observed that W^* does not affect the characteristics of the vertical thermal boundary layer. The isotherms on the horizontal layer are widely spaced for this lower value of T^*. The variation of Nusselt number with W^* is presented in Fig. 7. $W^* = 0$ corresponds to the classical problem of single vertical surface. The calculated value of Nu_v in the present study is 15.52. For $Pr = 0.72$, the similarity solution for Nu_v given by Gebhart *et al.* [12] is 15.04 and the correlation of Churchill and Chu [13] gives $Nu_v = 15.53$. The vertical surface Nusselt number decreases with increase in W^*. The initial drop in Nu_v is essentially due to the obstruction to fluid entrainment from bottom than due to preheating of the cold fluid by the horizontal surface. With further increase in W^*, the change in Nu_v is

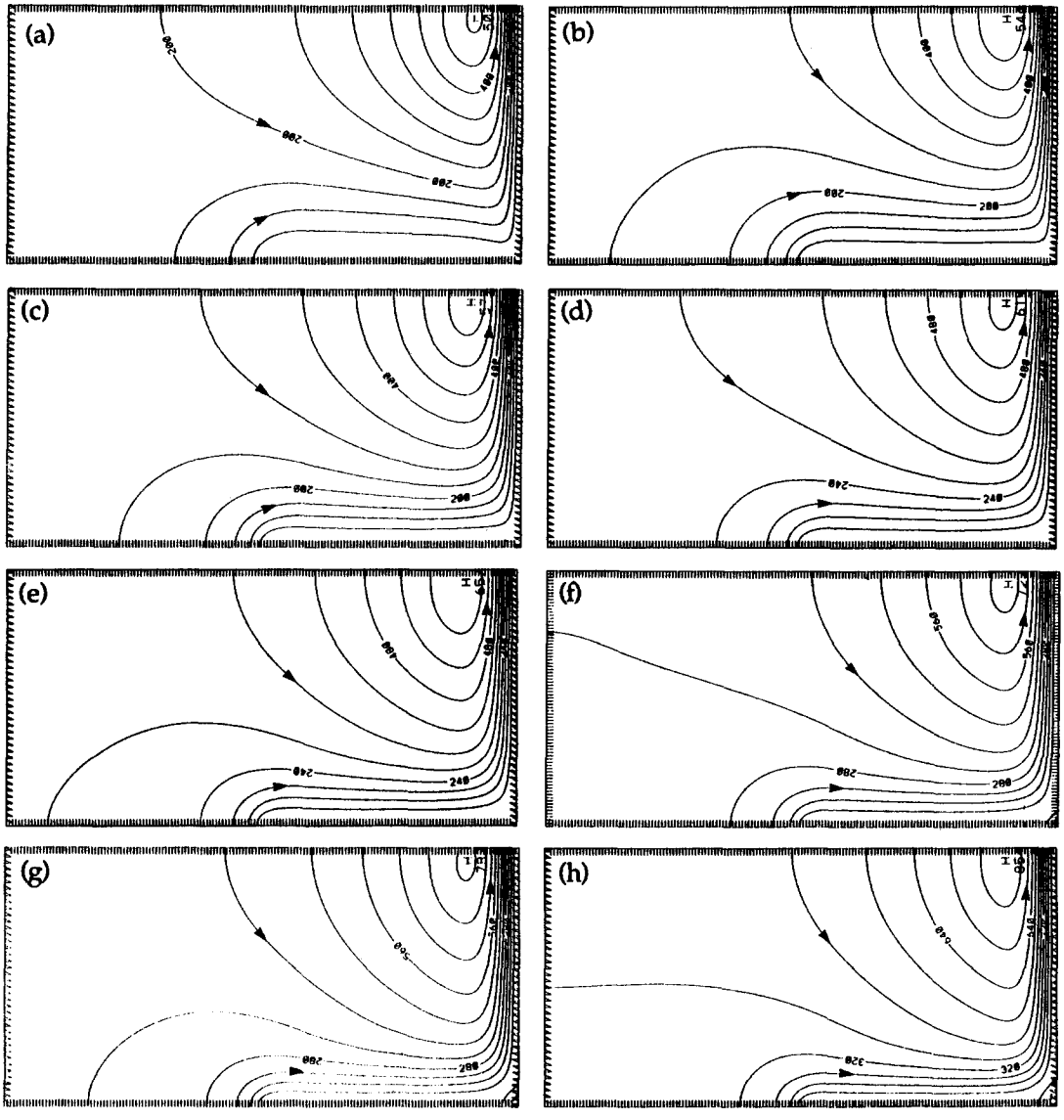

Fig. 2. Stream function contours for $Gr = 10^6$, $Pr = 0.7$ and $W^* = 1.0$. $T^* = 0.1$ (a), 0.3 (b), 0.5 (c), 0.75 (d), 1.0 (e), 1.5 (f), 2.0 (g) and 3.0 (h). $\psi_{wall} = 0$. $\Delta\psi = 50 \times 10^{-4}$ (a)–(c), 60×10^{-4} (d) and (e), 70×10^{-4} (f) and (g) and 80×10^4 (h).

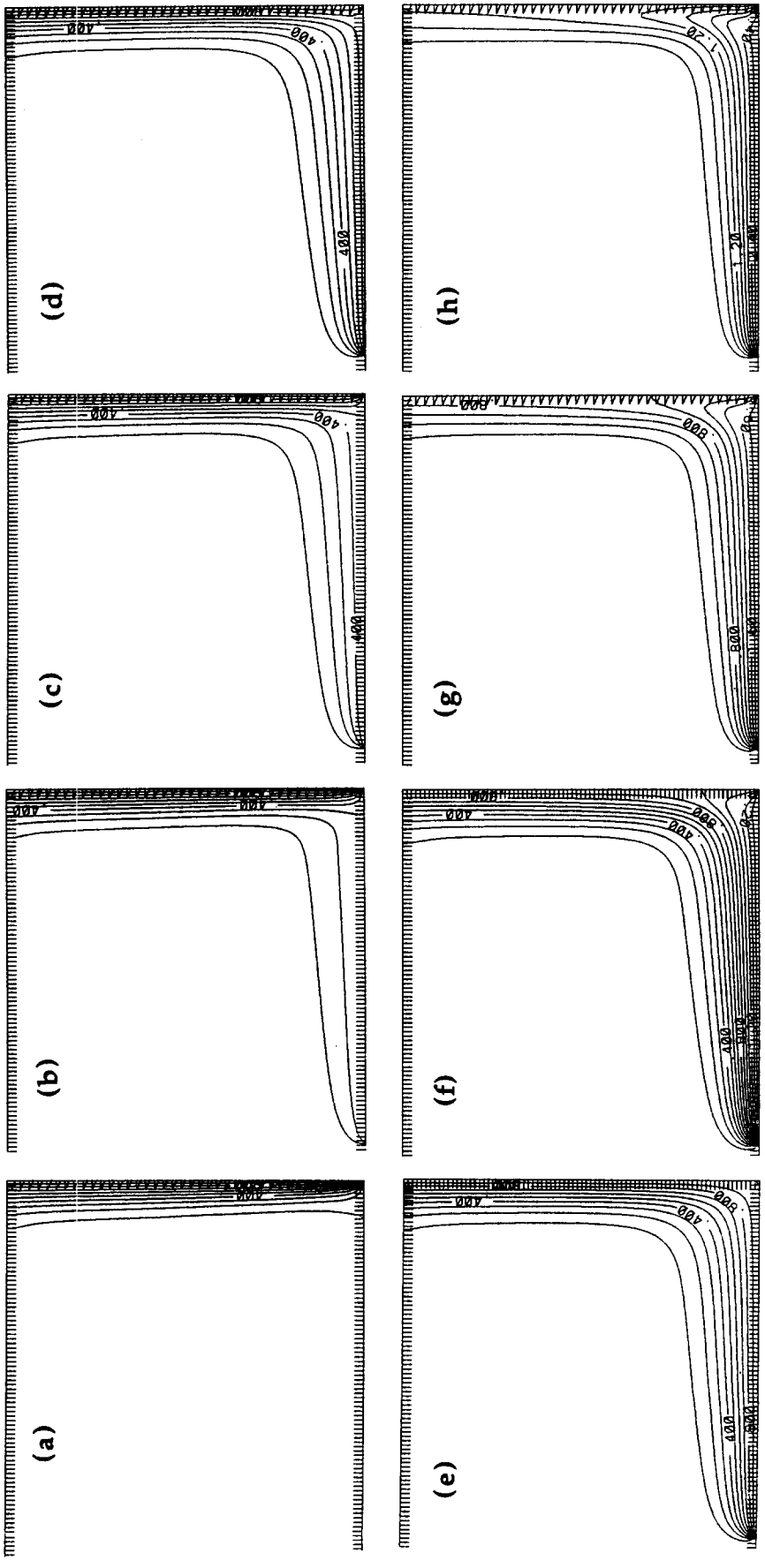

Fig. 3. Isotherms for $Gr = 10^6$, $Pr = 0.7$ and $W^* = 1.0$. $T^* = 0.1$ (a), 0.3 (b), 0.5 (c), 0.75 (d), 1.0 (e), 1.5 (f), 2.0 (g) and 3.0 (h). $\Delta T = 0.1$ (a)–(f), 0.2 (g) and 0.3 (h).

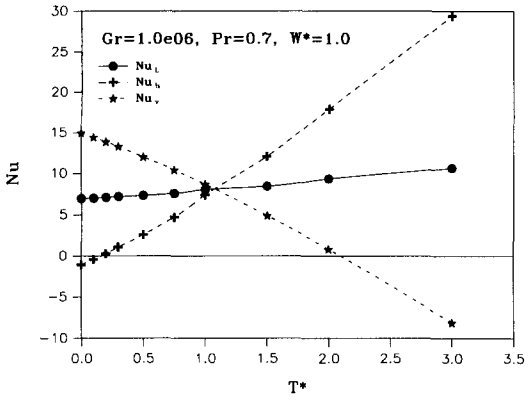

Fig. 4. Variation of Nusselt number with T^* for $Gr = 10^6$, $Pr = 0.7$ and $W^* = 1.0$.

smaller. Note that, in general, the effect of preheating on Nu_v is not substantial because $T^* = 0.5$.

The flow and transport observed for $T^* = 2.0$ for large W^* indicate some interesting features. For $W^* < 1.0$, Gr and Pr are the same as those for $T^* = 0.5$. For larger W^*, the value of Gr is chosen to be 10^4 to ensure that the laminar flow assumption is valid. Figure 8 shows stream function contours for $T^* = 2.0$ and $0.1 \leqslant W^* \leqslant 0.75$. The entrainment characteristics are essentially the same as those for $T^* = 0.5$. Fluid flow, however, increases over the horizontal surface because of the much larger buoyancy. A small stagnation–recirculating zone is observed at the corner for the reasons explained previously. The corresponding isotherm contours are plotted in Fig. 9. The temperature gradients on the horizontal surface are steeper while those on the vertical are shallower. This is physically anticipated because of the higher temperature of the horizontal surface. The large preheating of the fluid as it flows over the horizontal surface further reduces the temperature gradients on the vertical surface. A portion of the vertical surface near the corner gains heat, and its extent increases with increasing W^*.

The variation of Nusselt number with W^* for $T^* = 2.0$ is shown in Fig. 10. Nu_v as expected decreases with increase in W^*. The initial drop in Nu_v is again observed to be significant. This change is due to blocking as well as preheating of the cold fluid entraining from bottom by the horizontal surface. Of these two effects, preheating plays a dominant role because of the higher value of the horizontal surface temperature. On the other hand, Nu_h increases with increase in W^* because of larger surface area available for heat transfer.

The Grashof number based on the height and temperature of the vertical surface may not truly characterize the buoyant convection over the horizontal surface. For a large W^* and T^*, the effective Grashof number for the flow over the horizontal surface will be substantially larger than Gr, and the flow may be turbulent. Since turbulent flows can not be modeled by the current analysis, a lower value of $Gr = 10^4$ is chosen to study the effect of a long horizontal surface with large T^*.

For symmetric heating of the corner, it was shown [9] that initially a plume forms at the leading edge of the corner. The vertical boundary layer ultimately dominates the flow, and the plume merges with the vertical wall layer flow. A steady pattern develops in which the fluid flows over the horizontal surface, turns, then washes the vertical surface. No plume is observed after steady flow is established. For asymmetric heating with larger horizontal surface temperature, a steady plume flow develops on the horizontal surface if W^* is sufficiently large. For example, for $T^* = 2.0$, and $Ra = 0.7 \times 10^4$ a steady plume is observed on the horizontal surface when $W^* = 2$. In Fig. 11, stream function contours are shown for $W^* = 3$. The entraining downdraft is sandwiched between the vertical plume and the wall boundary layer flows. Further entrainment for the plume is drawn from below the horizontal surface. The steady plume is located where the strength of the plume buoyancy and the pull of the vertical wall boundary layer are in dynamic balance.

The corresponding isotherm contours are shown in Fig. 12. Because of the plume growth, the temperature gradients on the horizontal surface are weaker. We also notice that the area of the vertical surface receiving heat from the preheated fluid has substantially increased. The pool of fluid lying on the horizontal surface between the two vertical flows is almost stagnant. Heat transfer through this layer of fluid is mostly by conduction.

Nusselt number data are presented in Table 1. The top portion of the vertical surface loses heat while the bottom portion gains it. The net effect is heat transfer to the vertical surface.

3.3. *Effect of Prandtl number*

Three values of Prandtl number, 0.7, 7.0 and 70.0, are chosen for $Gr = 10^4$, $W^* = 2.0$ and $T^* = 2.0$ to study its effect on flow and heat transfer. Significant differences in flow and thermal fields are observed. Steady-state solutions have been obtained for $Pr = 0.7$, and 7.0, while the flow remained unsteady for $Pr = 70$.

Figure 13 shows the stream function plots of steady flows. A steady vertical plume grows near the horizontal leading edge in each case. The downdraft between the plume and the wall boundary layer is wide and has lower velocities. The downdraft feeds the entrainment for both the vertical buoyant flows. The fluid layer over the horizontal surface is almost stagnant and heat transfer through this layer occurs essentially by conduction as demonstrated by nearly horizontal isotherms (Fig. 14). In Fig. 14 the isotherms for $Pr = 0.7$ are seen to be widely spaced compared to $Pr = 7.0$ indicating larger thermal dispersion in gases relative to liquids.

At much higher value of Pr (= 70.0), the flow remains unsteady. Transient stream function contours

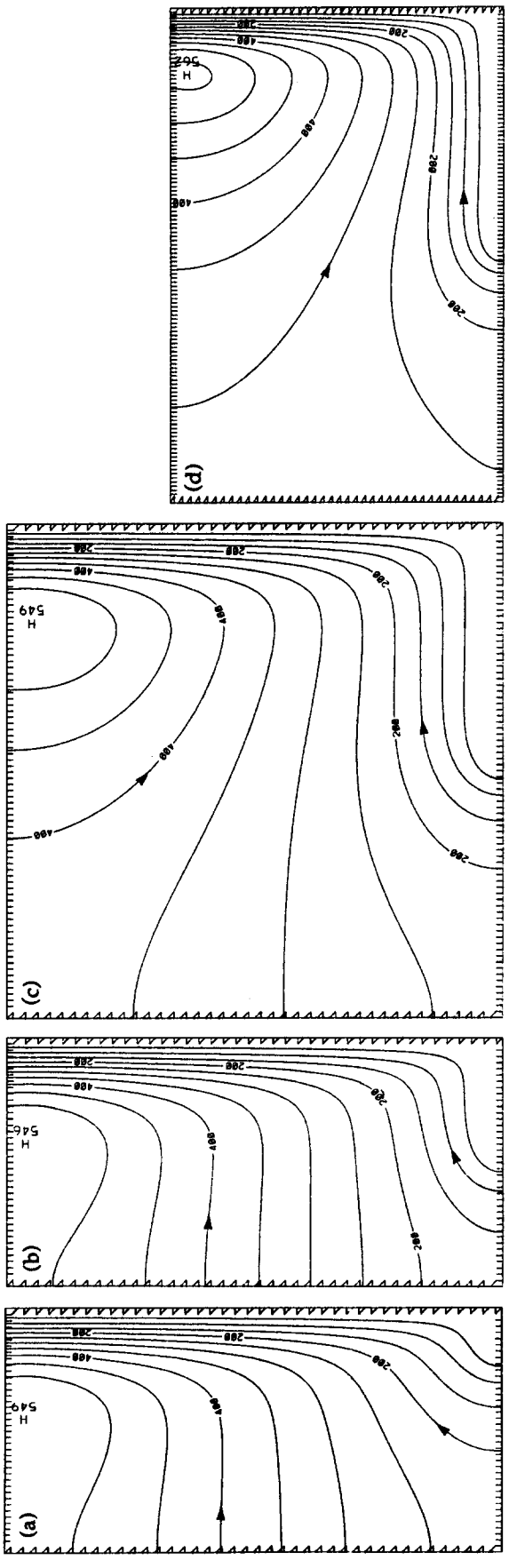

Fig. 5. Stream function contours for $Gr = 10^6$, $Pr = 0.7$ and $T^* = 0.5$. $W^* = 0.1$ (a), 0.25 (b), 0.5 (c) and 0.75 (d). $\psi_{\text{wall}} = 0$. $\Delta\psi = 50 \times 10^{-4}$.

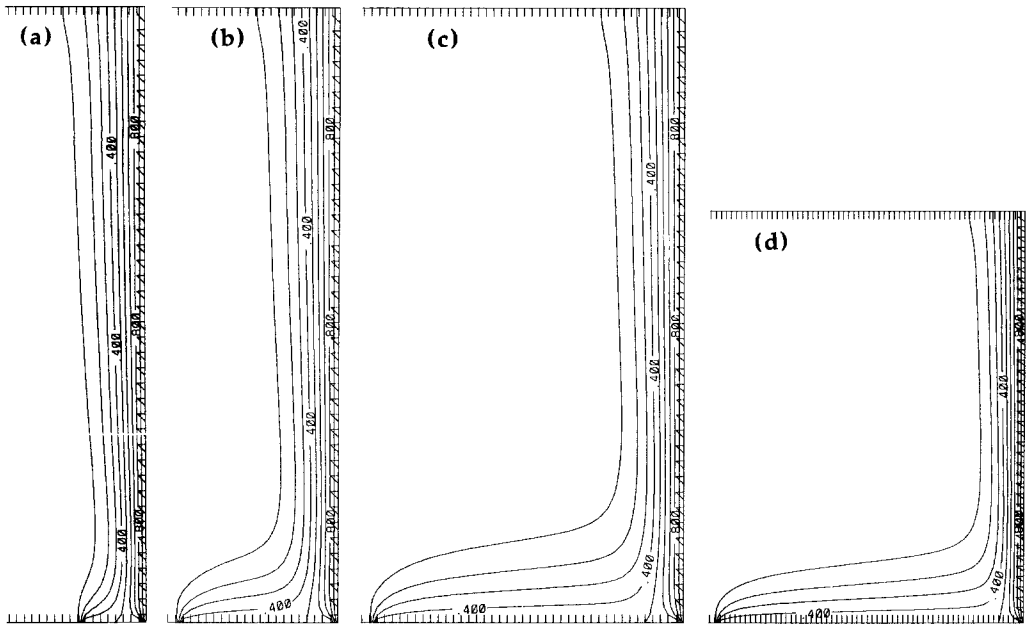

Fig. 6. Isotherms for $Gr = 10^6$, $Pr = 0.7$ and $T^* = 0.5$. $\Delta T = 0.1$. $W^* = 0.1$ (a), 0.25 (b), 0.5 (c) and 0.75 (d).

and isotherms are presented in Figs. 15 and 16, respectively. As in [9], the corner is impulsively heated with no initial flow and heat transfer, and a plume begins to grow near the leading edge of the surface. The vertical wall boundary layer develops independent of the plume by drawing entrainment from the top. Since the Prandtl number is very large, thermal dispersion in these flows is very small facilitating the independent growth of the plume and vertical wall layer. Further heat loss from the horizontal surface springs up a second plume between the two vertical flows. Recall that two other factors, $W^* = 2.0$ and $T^* = 2.0$ contribute to this, besides the large Prandtl number. The second plume introduces instability in the flow because the three vertical flows compete for entrainment flow to sustain themselves. The wall boundary layer remains strong and eventually wins the competition. In this process, the plume at the leading edge shifts towards the wall, and the plume near the wall merges with the wall flow. Multiple plumes continue to grow along the length of the horizontal surface, each shifting towards the vertical wall. Thus an unsteady flow pattern of ripples formation and merger with the vertical wall boundary layer establishes. In the absence of the vertical wall, we expect the plumes to grow vertically upwards. This was demonstrated through experiments in water by Sparrow *et al.* [14] and Adrian *et al.* [15].

Significant differences are observed in the values of the Nusselt numbers as shown in Table 2. The Nusselt numbers for $Pr = 70$ are obtained by time-averaging after the initial instabilities.

4. FLOW VISUALIZATION

The objective of this experimental investigation is to verify the flow patterns observed in the numerical study. Experiments were performed in air for two values of T^*, 0.5 and 2.0, with different aspect ratio. Some of the representative results are presented in this section.

4.1. *Apparatus details*

Both the horizontal and vertical surfaces of the corner [Fig. 17(a)] are made of copper. The span-wise width of the L-corner is 12.70 cm, and the height of the vertical surface is 10.16 cm. The thickness of each plate is 0.625 cm. Three holes of diameter 0.144 cm and depth 0.3175 cm were drilled on the back of the vertical surface to accommodate the thermocouples, see Fig. 17(b). These holes are located on the central vertical line at 2.54 cm, 5.08 cm and 7.62 cm distance from the top of the vertical surface. Locating the thermocouples at different heights makes it possible to check the isothermality of the vertical surface. Grooves of width 0.0678 cm were machined hori-

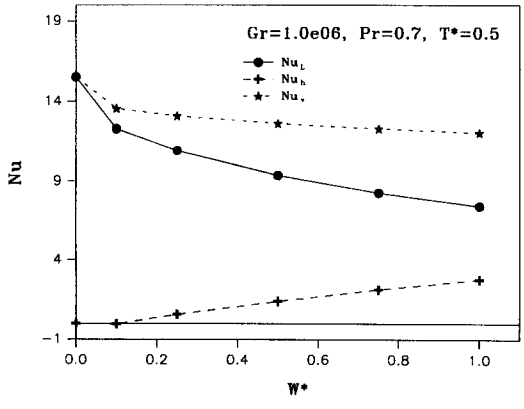

Fig. 7. Nusselt number variation with W^* for $Gr = 10^6$, $Pr = 0.7$ and $T^* = 0.5$.

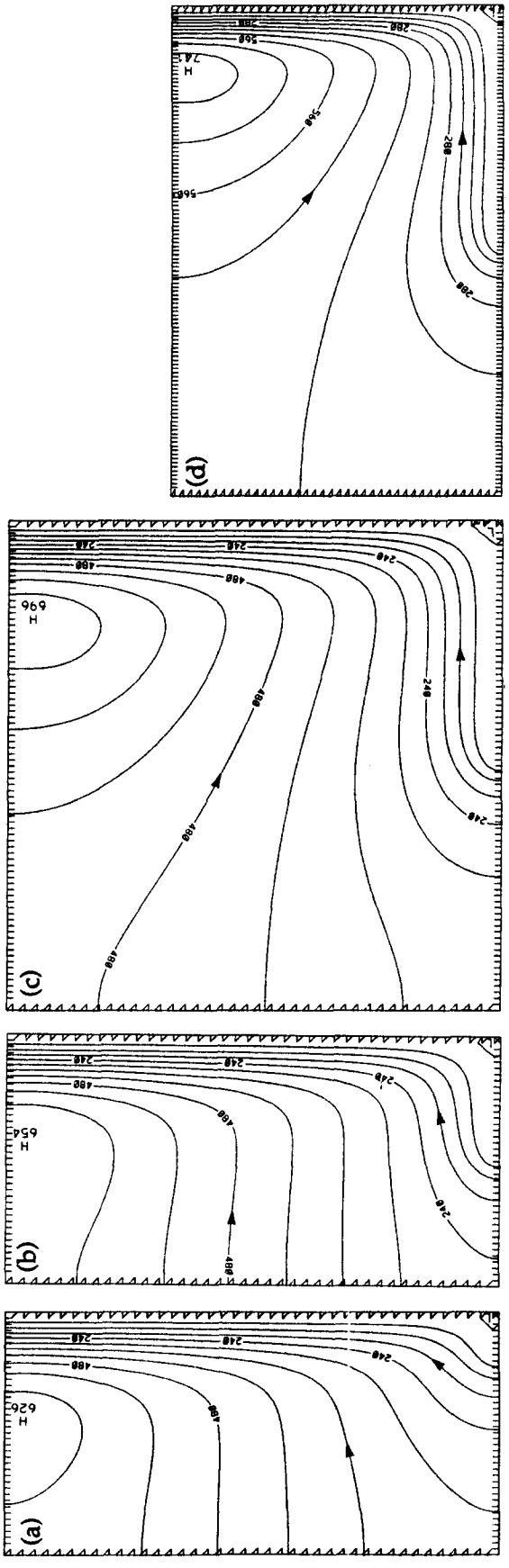

Fig. 8. Stream function contours for $Gr = 10^6$, $Pr = 0.7$ and $T^* = 2.0$. $W^* = 0.1$ (a), 0.25 (b), 0.5 (c) and 0.75 (d). $\psi_{wall} = 0$. $\Delta\psi = 60 \times 10^{-4}$ (a)–(c) and 70×10^{-4} (d).

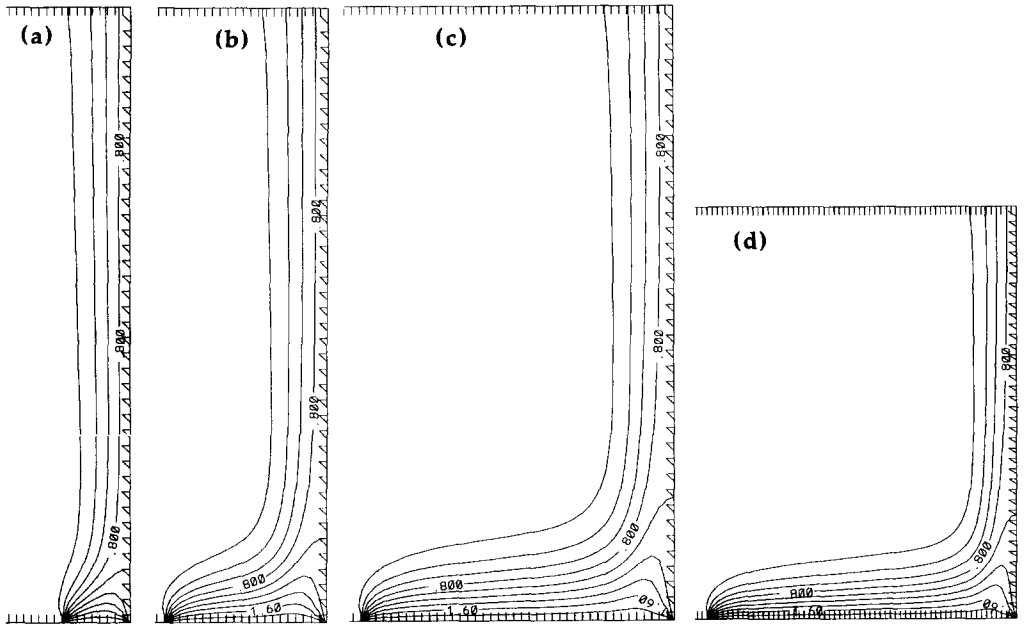

Fig. 9. Isotherms for $Gr = 10^6$, $Pr = 0.7$ and $T^* = 2.0$. $\Delta T = 0.2$. $W^* = 0.1$ (a), 0.25 (b), 0.5 (c) and 0.75 (d).

zontally from the holes to one end to accommodate the thermocouple wire.

To generate corners of different aspect ratios, the horizontal surface was made of several sections which can be modularly combined. These sections consist of one 3.175 cm long plate, three 2.54 cm long plates, and four 5.08 cm long plates. They can be arranged to give aspect ratios of 0.25, 0.5, 0.75, 1.0, 1.5, 2.0 and 3.0. The 3.175 cm long plate and the vertical plate were assembled at 90° by using three plastic screws. These plastic screws minimize the possibility of heat transfer from one surface to another. Holes and grooves were cut on the back side of every other section of the horizontal surface in a way similar to that for the vertical surface. A schematic diagram of assembly procedure used for the horizontal surface is shown in Fig. 17(c). Two dowel pins were provided on one of the sides of each section on the horizontal surface. These pins fit into the corresponding holes provided on the side of the adjacent plate when they are assembled. The dowel pins assure proper alignment between the surfaces. Two holes were drilled through these sections along their length, and a threaded rod passes through them. The joint between the sections was made air tight by tightening the nut on the threaded rod.

The wall temperatures were measured with a fine-gauge Teflon insulated copper–constantan thermocouples fixed in the holes by using a highly thermal conductive epoxy adhesive. The epoxy was cured at 120°C for 8 h. Wire-wound silicone rubber flexible heaters were fixed to the back side of the plates using vulcanizing (RTV) silicone adhesive which was cured for 24 h at room temperature. Electric power was supplied to the heaters through powerstats which allowed control of power input to the heaters. The assembled L-corner was placed on an insulation board made of fiber glass of 5.08 cm thickness. To minimize the end effects, the front and the back ends were closed with Plexiglas [see Fig. 18(a)].

Two different insulating materials were used to prevent unwanted heat loss. Close-pored Styrofoam was used on the back side of each surface to prevent any heat loss to the environment. The insulation is 5.08 cm thick and recesses were machined into the facing surface to accommodate the heated plates as shown in Fig. 17(a). Insulation was extended by 5.08 cm on both sides of the surface to prevent extraneous heat transfer from the sides. A thin insulating material, made of fiber glass is used at the interface of the horizontal and the vertical plates to prevent heat transfer from one plate to the other. This arrangement

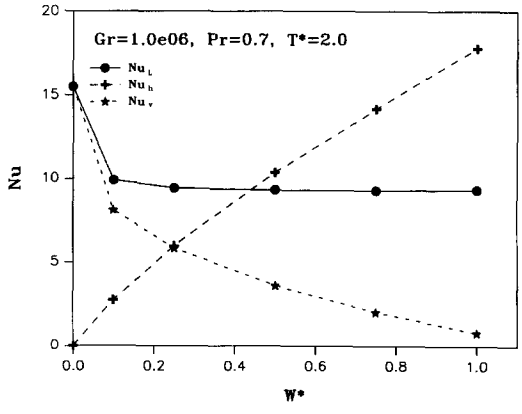

Fig. 10. Nusselt number variation with W^* for $Gr = 10^6$, $Pr = 0.7$ and $T^* = 2.0$.

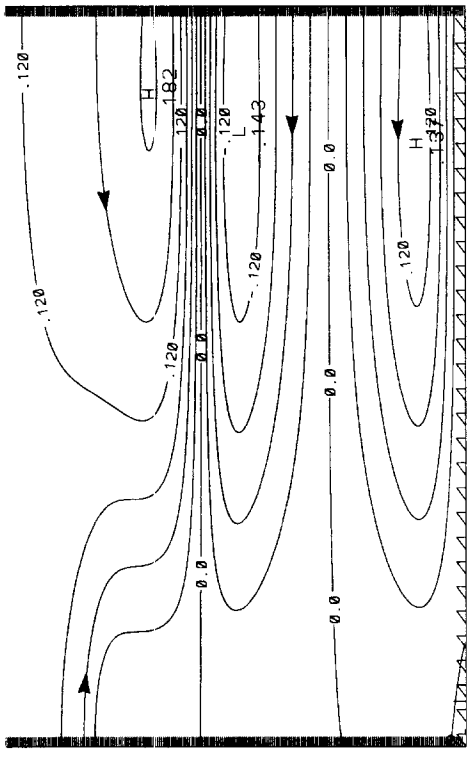

Fig. 11. Stream function contours for $W^* = 3.0$, $T^* = 2.0$, $Pr = 0.7$ and $Gr = 10^4$. $\psi_{wall} = 0$.

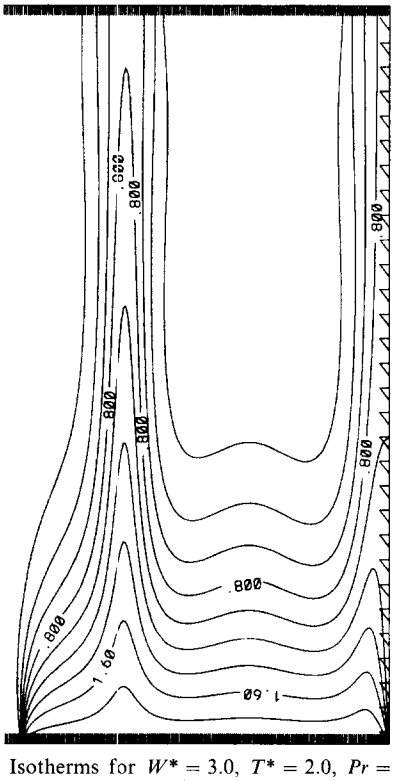

Fig. 12. Isotherms for $W^* = 3.0$, $T^* = 2.0$, $Pr = 0.7$ and $Gr = 10^4$. $\Delta T = 0.2$.

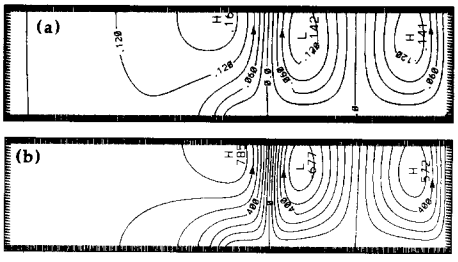

Fig. 13. Stream function plots for $Gr = 10^4$, $W^* = 2.0$ and $T^* = 2.0$. $Pr = 0.7$ (a) and 7.0 (b). Contour values scaled by 10^4.

allows to maintain the horizontal and vertical surfaces at different temperatures.

4.2. *Flow visualization*

Smoke used for flow visualization was generated by passing air through a bulb which contained cotton soaked in titanium tetra chloride ($TiCl_4$). $TiCl_4$ reacts with the moisture in air and produces TiO_2 and HCl. The chemical TiO_2 is a dense white gas. The air flow is controlled by using a pneumatic flow controller. The air is passed through a series of tubes with gradually increasing diameters. The last tube has small diameter holes (nozzles) drilled along its length and is located near the bottom of the insulation board. The other end of this tube is closed so that smoke emerges through the holes into the corner.

4.3. *Data acquisition*

The thermocouples were connected to a terminal board which has a built-in circuitry for cold junction compensation. The terminal board is connected to a data-acquisition board which amplifies, compares and processes the signals from the thermocouples and the cold junction compensation circuit. The digital signal from the data-acquisition board was fed to a computer which displayed the temperature readings. The signal from each thermocouple was read once in 81 ms.

4.4. *Experimental procedure*

The L-corner assembly was placed in a chemical hood and was totally isolated from the disturbances in the environment. The heaters were connected to the power source through powerstats. The powerstats were adjusted to reach the steady-state surface temperature required to achieve a given value of Grashof

Table 1. Nusselt number for various values of W^* with $Gr = 10^4$, $Pr = 0.7$ and $T^* = 2.0$

W^*	Nu_v	Nu_h	Nu_L
1.75	−2.89	12.486	3.49
2.0	−1.52	16.88	5.12
3.0	−1.44	19.53	4.52

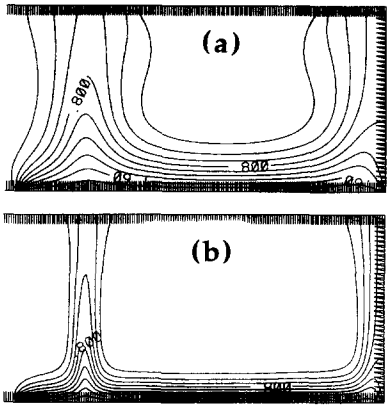

Fig. 14. Isotherms for $Gr = 10^4$, $W^* = 2.0$ and $T^* = 2.0$. $Pr = 0.7$ (a) and 7.0 (b).

number. Steady-state was assumed to have been reached when the variation in surface temperature was within ± 0.5°C in 1 h. Once steady-state was attained, smoke was introduced into the corner in the manner described above and pictures of the flow patterns were taken.

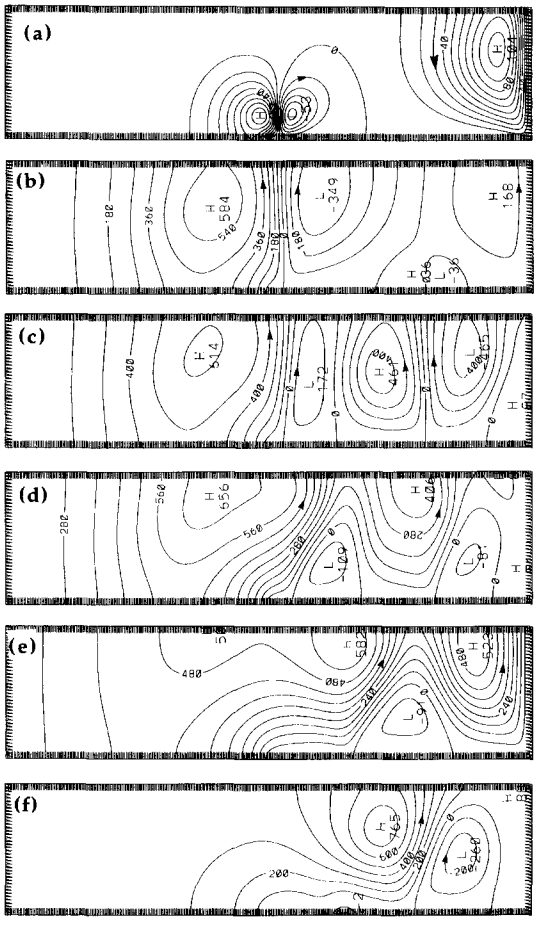

Fig. 15. Transient stream function contours for $Pr = 70$, $Gr = 10^4$, $W^* = 2.0$ and $T^* = 2.0$. Contour values scaled by 10^4. $\tau^* = 10$ (a), 30 (b), 40 (c), 50 (d), 70 (e) and 90 (f).

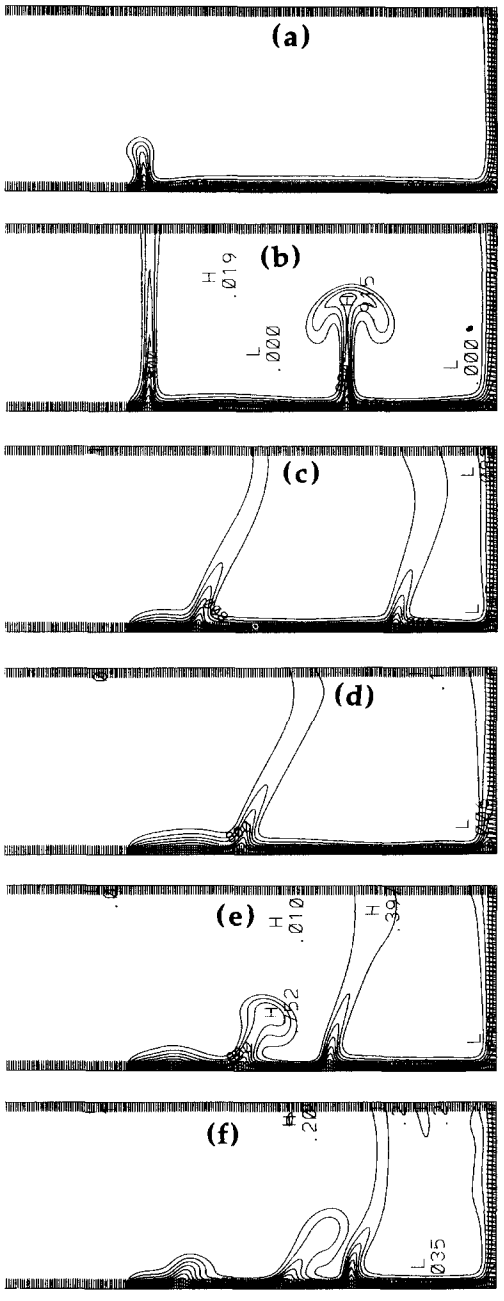

Fig. 16. Transient isotherms for $Pr = 70$, $Gr = 10^4$, $W^* = 2.0$ and $T^* = 2.0$. $\tau^* = 10$ (a), 35 (b), 60 (c), 70 (d), 85 (e) and 95 (f).

5. RESULTS AND DISCUSSION

Experiments were performed for three values of T^*; 0.5, 1.0 and 2.0. In all the experiments, flow patterns show the fluid entrainment from the bottom. They do not reveal any fluid entrainment from the top because no smoke was injected there.

For $T^* = 1.0$, experiment was conducted for a square corner ($W^* = 1.0$) to compare the flow patterns with those presented by Ruiz and Sparrow [8]. For this case, the horizontal and vertical surfaces were maintained at 34°C and t_∞ was 22°C. The calculated

Table 2. Nusselt number for the corner, and for horizontal and vertical surfaces with $Gr = 10^4$ $T^* = 2.0$ and $W^* = 2.0$

Pr	Nu_L	Nu_h	Nu_v
0.7	5.12	16.88	−1.52
7.0	10.25	29.73	1.01
70.0	22.54	60.76	6.84

Gr value for the surfaces is 1.6×10^6. The flow pattern is presented in Fig. 18(a). Flow is slightly unsteady over the horizontal surface. Fluid entering from the bottom flows over the horizontal surface before it bends and enters the vertical layer. This observation is in good agreement with the numerical results presented in [9] and the experimental flow pattern presented in [8].

For $T^* = 0.5$, flow patterns were studied for three values of W^*, 0.25, 0.5 and 1.0. For this set, the horizontal and vertical surfaces are respectively maintained at 33.6 and 44°C. The calculated Gr for the vertical surface is 2.5×10^6. The flow patterns are presented in Fig. 18(b)–(d) for $W^* = 0.25$, 0.5 and 1.0, respectively. For the three values of W^*, flow is observed to be steady. Fluid entraining from the bottom flows over the horizontal surface before it enters the vertical layer. For $W^* = 0.5$, a region of low velocities is observed on the horizontal surface. It is observed that the vertical layer remains attached to the surface of the insulation which extends vertically upward from the heated vertical surface. This flow pattern justifies the numerical boundary condition which assumes that the fluid leaves the computational domain vertically.

For $T^* = 2.0$, the observed flow patterns are presented for $W^* = 1.0$ and 1.5, see Fig. 18(e) and (f). The horizontal and the vertical surfaces were held at 43.4 and 33°C, respectively. The calculated Gr values for $W^* = 1.0$ and 1.5 are 3.2×10^7 and 1.09×10^8, respectively. Flows were observed to be unsteady in both the cases. However, snap-shots of the typical flow patterns shown in Fig. 18(e) and (f) are very similar to the numerical simulations shown before. Note that, for $W^* = 1.5$, the fluid entering from the bottom does not reach the vertical layer. Instead, it rises off the horizontal surface and forms an unsteady plume. The vertical layer is mostly fed by the fluid entraining from the top (see Fig. 11). This, however, can not be observed in plate 6 because, as mentioned earlier, no smoke was injected at the top.

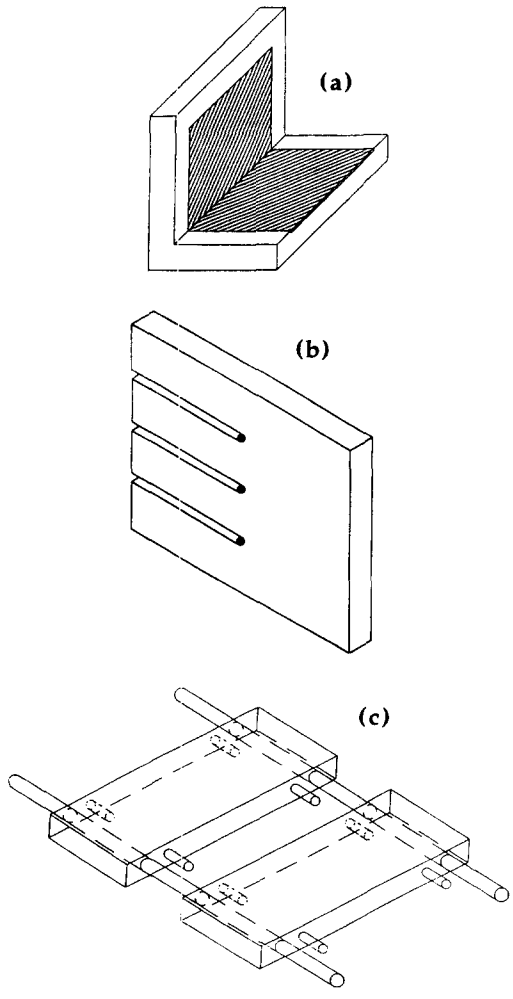

Fig. 17. Experimental setup: (a) schematic diagram, (b) arrangement of thermocouples and (c) assembly of the horizontal surface.

6. CONCLUSIONS

We have reported numerical simulations and experimental flow visualizations of buoyancy-induced flow and heat transfer from isothermal L-shaped corners with asymmetric heating. The salient results of the study are summarized below.

(1) Increasing the horizontal surface temperature (T^*) decreases the heat transfer rate from the vertical surface. For sufficiently large T^*, there is a net heat gain by the vertical surface.

(2) For longer horizontal surfaces, the entrainment for the vertical boundary layer shifts from the side to the top. The horizontal flow always entrains from below.

(3) A steady plume forms on the horizontal surface for large T^* and W^*.

(4) The influence of Prandtl number on flow and heat transfer is significant. For high Prandtl number, unsteady flows occur with multiple plumes on the horizontal surface. The heat transfer rates are substantially enhanced for a higher Prandtl number.

(5) Flow visualizations with smoke-injection support the entrainment characteristics obtained by numerical simulations.

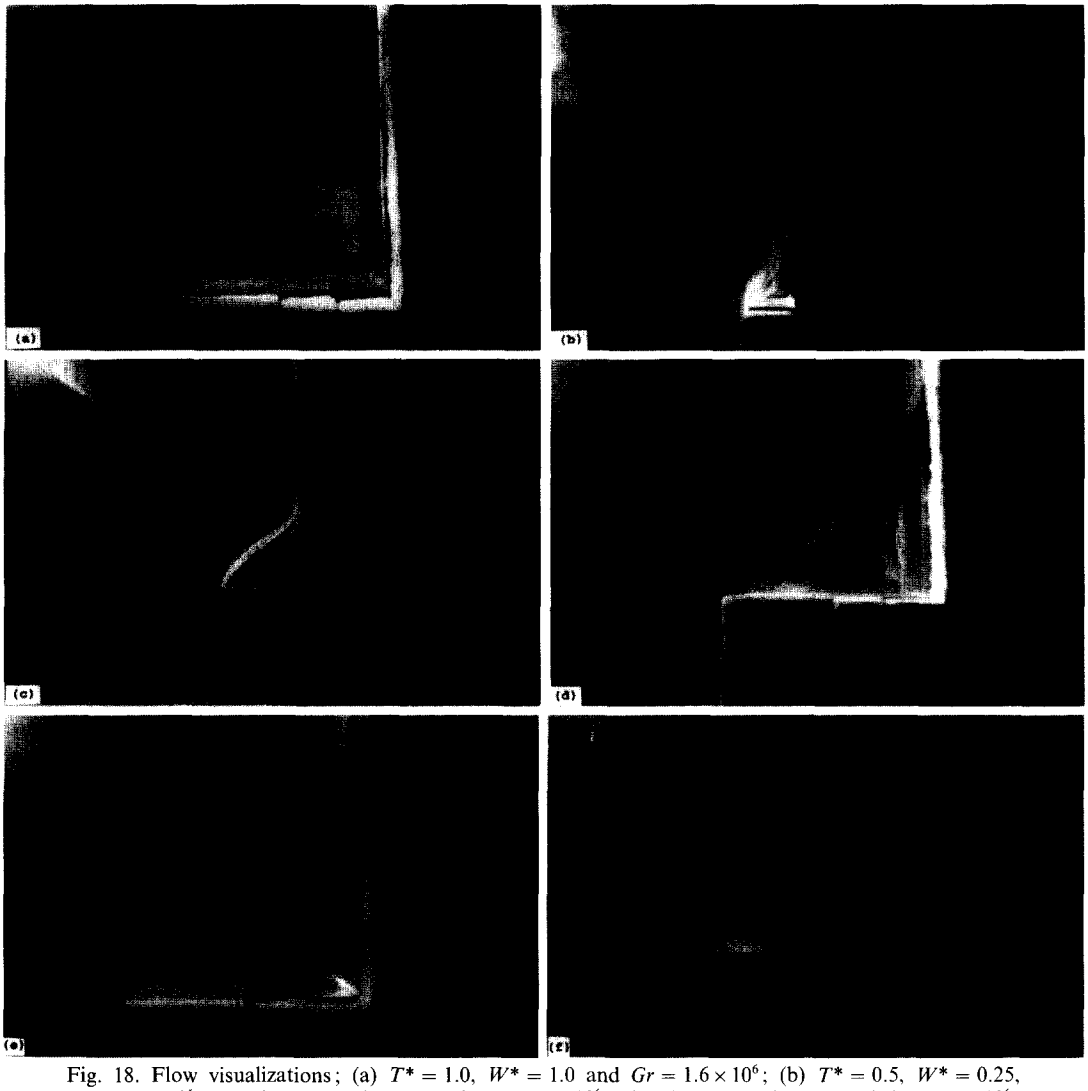

Fig. 18. Flow visualizations; (a) $T^* = 1.0$, $W^* = 1.0$ and $Gr = 1.6 \times 10^6$; (b) $T^* = 0.5$, $W^* = 0.25$, $Gr = 2.5 \times 10^6$; (c) $T^* = 0.5$, $W^* = 0.5$ and $Gr = 2.5 \times 10^6$; (d) $T^* = 0.5$, $W^* = 1.0$ and $Gr = 2.5 \times 10^6$; (e) $T^* = 2.0$, $W^* = 1.0$ and $Gr = 3.2 \times 10^7$ and (f) $T^* = 2.0$, $W^* = 1.5$ and $Gr = 1.09 \times 10^8$.

Acknowledgement—The authors gratefully acknowledge the partial funding support provided by the Center for Advanced Manufacturing and Packaging of Microwave, Optical and Digital Electronics (CAMPmode).

REFERENCES

1. D. Angirasa and R. L. Mahajan, Natural convection from L-shaped corners with adiabatic and cold isothermal horizontal walls, *J. Heat Transfer* **115,** 149–157 (1993).
2. C. Rodighiero and L. M. de Socio, Some aspects of natural convection in a corner, *J. Heat Transfer* **105,** 212–214 (1983).
3. P. Luchini, Analytical and numerical solutions for natural convection in a corner, *AIAA J.* **24,** 841–848 (1986).
4. Y. Jaluria, Interaction of natural convection wakes arising from thermal sources on a vertical surface, *J. Heat Transfer* **107,** 883–892 (1985).
5. D. B. Ingham and I. Pop, A note on free convection flow in a corner, *Int. Commun. Heat Transfer* **15,** 315–321 (1988).
6. D. B. Ingham and I. Pop, Natural convection in a right-angle corner: higher order analysis, *Int. J. Heat Mass Transfer* **32,** 2167–2177 (1989).
7. D. B. Ingham and I. Pop, A higher order analysis of natural convection in a corner, *Wärme- und Stoffübertragung* **26,** 289–298 (1991).
8. R. Ruiz and E. M. Sparrow, Natural convection in V-shaped and L-shaped corners, *Int. J. Heat Mass Transfer* **30,** 2539–2548 (1987).
9. D. Angirasa, R. B. Chinnakotla and R. L. Mahajan, Buoyancy-induced convection from isothermal L-shaped corners with symmetrically heated surfaces, *Int. J. Heat Mass Transfer* **37,** 2439–2463 (1994).
10. P. J. Roache, *Computational Fluid Dynamics*. Hermosa, Albuquerque, NM (1982).
11. W. H. Press, S. A. Teukolsky, W. T. Vetterling and B. P. Flannery, *Numerical Recipes: The Art of Scientific*

Computing (2nd Edn). Cambridge University Press, New York (1992).
12. B. Gebhart, Y. Jaluria, R. L. Mahajan and B. Sammakia, *Buoyancy-Induced Flows and Transport*. Hemisphere, Washington DC (1988).
13. S. W. Churchill and H. H. S. Chu, Correlating equations for laminar and turbulent free convection from a vertical plate, *Int. J. Heat Mass Transfer* **18,** 1323–1329 (1975).
14. E. M. Sparrow, R. B. Husar, and R. J. Goldstein, Observations and other characteristics of thermals, *J. Fluid Mech.* **41,** 793–800 (1970).
15. R. J. Adrian, R. T. D. S. Ferreira and T. Boberg, Turbulent thermal convection in wide horizontal fluid layers, *Exp. Fluids* **4,** 121–141 (1986).